



1 Response of Coastal California Hydroclimate to the Paleocene-

Eocene Thermal Maximum

- 3 Xiaodong Zhang^{1*}, Brett J. Tipple², Jiang Zhu³, William D. Rush⁴, Christian A. Shields³, Joseph
- 4 B. Novak⁵, James C. Zachos¹
- 5 Department of Earth and Planetary Sciences, University of California, Santa Cruz, CA 95064, USA
- 6 ²FloraTrace Inc., Salt Lake City, UT 84103, USA
- 7 3Climate and Global Dynamics Laboratory, National Center for Atmospheric Research, Boulder, CO 80307, USA
- 8 Department of Environmental Studies and Sciences, Santa Clara University, Santa Clara, CA 95053, USA
- 9 ⁵Department of Ocean Sciences, University of California, Santa Cruz, CA 95064, USA
- ***Correspondence to: Xiaodong Zhang (xzhan335@ucsc.edu)
- 11 **Abstract.** The effects of anthropogenic warming on the hydroclimate of California are becoming
- more pronounced, with increased frequency of multi-year droughts and flooding. As a past
- analog for the future, the Paleocene-Eocene Thermal Maximum (PETM) is a unique natural
- 14 experiment for assessing global and regional hydroclimate sensitivity to greenhouse gas
- warming. Globally, extensive evidence (i.e., observations, climate models with high pCO_2)
- demonstrates hydrological intensification with significant variability from region to region (i.e.,
- dryer or wetter, or greater frequency and/or intensity of extreme events). Central California
- 18 (paleolatitude ~42°N), roughly at the boundary between dry subtropical highs and mid-latitude
- 19 low pressure systems, would have been particularly susceptible to shifts in atmospheric
- 20 circulation and precipitation patterns/intensity. Here, we present new observations and climate
- 21 model output on regional/local hydroclimate responses in central California during PETM. Our
- 22 findings based on multi-proxy evidence within the context of model output suggest a transition to
- an overall drier climate punctuated by increased precipitation during summer months along the
- 24 central coastal California during the PETM.

25 1 Introduction





26 Global warming of a few degrees Celsius over the next century is projected to intensify the 27 hydrological cycle on a range of temporal and spatial scales, manifested primarily by amplified wet-dry cycles(Held and Soden, 2006; Douville et al., 2021). Indeed, just over last few decades 28 there has been an increasing frequency in the severity of extremes characterized by compound 29 heat waves and intense drought(Büntgen et al., 2021; Williams et al., 2020; Zscheischler and 30 31 Lehner, 2022), and/or heavy precipitation and flooding(Liu et al., 2020; Risser and Wehner, 2017). As greenhouse gas driven warming continues, such precipitation extremes (wet or dry) 32 are expected to intensify(Stevenson et al., 2022). 33 California, a region vulnerable to amplified wet-dry cycles, is already experiencing multiyear 34 extreme droughts with longer precipitation deficits interspersed with anomalously wet 35 years(Zamora-Reyes et al., 2022). For example, the prolonged drought from 2012 to 2016 36 preceded the exceptionally high numbers of atmospheric river storms-related winter flooding of 37 2017(Simon Wang et al., 2017). Collectively, climate models (e.g., CESM, CMIP etc.) show that 38 the occurrence of such extremes in droughts and excessive seasonal precipitation in California is 39 expected to increase by the end of the century (Vogel et al., 2020; Swain et al., 2018). In addition, 40 such 'whiplash' hydroclimate shifts related to anthropogenic warming are generally supported by 41 42 historical records of California climate cycles(de Wet et al., 2021; Polade et al., 2017). The most robust evidence for greenhouse warming-induced intensification of the hydrological 43 44 cycle comes from global warming events of the deep past(Carmichael et al., 2017). In particular, 45 the Paleocene-Eocene Thermal Maximum (PETM) has emerged as a unique natural experiment for assessing global and regional hydroclimate sensitivity to greenhouse gas warming(Zachos et 46 al., 2008). Extensive evidence exists for a major mode shift of local/regional precipitation 47 48 patterns and intensity(Pagani et al., 2006; Slotnick et al., 2012; Schmitz and Pujalte, 2003; Sluijs and Brinkhuis, 2009; Smith et al., 2007; Handley et al., 2012; Kozdon et al., 2020) including 49 enhanced erosion and extreme flooding in fluvial sections (e.g., Pyrenees; Bighorn basin), and 50 increased weathering and sediment fluxes to coastal basins (e.g., Bass River, Wilson Lake, mid-51 52 Atlantic coast; Mead Stream, New Zealand etc.) along with other observations(John et al., 2008; Nicolo et al., 2010; Stassen et al., 2012; Self-Trail et al., 2017; Wing et al., 2005; Kraus and 53 54 Riggins, 2007; Foreman, 2014).





55 These observations of regional hydroclimate change serve as the basis for climate model 56 experiments forced with proxy-based estimates of $\Delta p CO_2$ for the PETM (i.e., 3x-6x preindustrial)(Kiehl and Shields, 2013; Carmichael et al., 2016; Zhu et al., 2020). Using such 57 estimates, model simulations show an overall increase in poleward meridional water vapor 58 transport as manifested by a net increase in evaporation of subtropical regions, balanced by 59 60 higher precipitation of tropical/high latitudes characterizing the 'wet-gets-wetter and dry-getsdrier' hydrological response. The latest simulations using high-resolution climate models display 61 several key regional responses including increased frequency of extreme precipitation events, 62 especially the coastal regions where atmospheric rivers (AR) are common(Rush et al., 2021). 63 Indeed, observations of high-energy flooding events in SW Europe (i.e., the Pyrenees) during the 64 PETM(Schmitz and Pujalte, 2003) can be explained by increased frequency of North Atlantic 65 ARs contributing landfall in that region. Pacific AR activity as simulated for the PETM also 66 becomes more intense but less frequent along the central California coast by shifting northward 67 68 with the storm tracks(Shields et al., 2021), not unlike the projections for California in the future(Shields and Kiehl, 2016; Massoud et al., 2019). This pattern is consistent with warming 69 scenarios in general which have weakened zonal wind belts (i.e., the westerlies) that are shifting 70 71 poleward(Abell et al., 2021; Douville et al., 2021). Testing the theoretical response of Northeast Pacific ARs and seasonal precipitation along North 72 America's western coast in general is challenging and still limited by the lack of observations. 73 74 Here we constrain the regional hydroclimate response along the central California coast during the PETM using several independent proxies (i.e., clay mineralogy, grain size distribution, 75 $\delta^{13}C_{\text{org}}$ stratigraphy, and leaf wax $\delta^{2}H_{\text{n-alkane}}$ isotope records), which are either directly or 76 indirectly sensitive to shifts in precipitation patterns/intensity. These proxies are then compared 77 78 against sophisticated Earth System model simulations of the PETM climate to characterize the relative changes in regional precipitation (i.e., pattern/intensity). The new records complement 79 data from a previous study (John et al., 2008), and along with the latest climate modeling 80 experiments provide a unique case study of the sensitivity of regional hydroclimate to major 81 greenhouse warming. 82

2 Materials and methods





2.1 Site Location

The studied outcrop section is part of the late Paleocene-early Eocene Lodo Formation located in the Panoche Hill of central California (Fig. 1). During the late Paleocene, the section was situated at a paleolatitude \sim 42°N, roughly at the boundary between the dry subtropical highs and mid-latitude low-pressure systems. The Lodo Formation is comprised primarily of siltstone with a relatively low abundance of calcareous microfossils truncated by thin glauconitic sand layers(Brabb, 1983). Depositional facies are consistent with neritic-bathyal setting along the outer shelf(John et al., 2008).

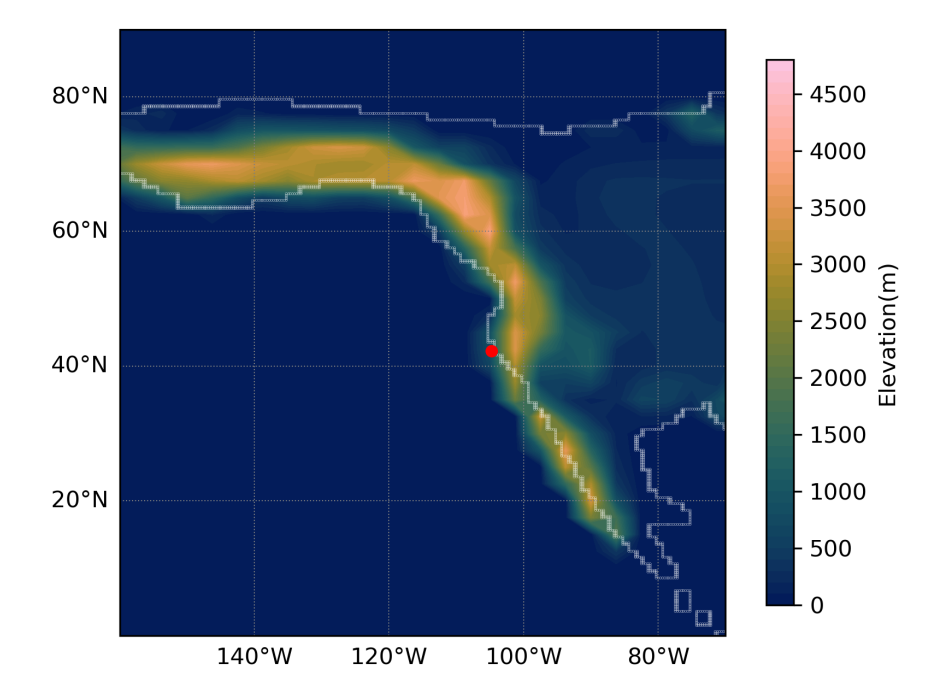


Figure 1. Paleogeography and location of the Lodo Gulch section (red spot) along the Pacific coast at 56 Ma. Late Paleocene-early Eocene topography of North America is adapted from Lunt et al. (2017).





- 97 2.2 Methods
- 98 2.2.1 Stable isotopes
- 99 Sediment samples used for this study include those originally collected by John et al. (2008). In
- addition, new samples were collected from the upper Paleocene for organic C isotopic analysis to
- 101 better establish pre-PETM baseline. Samples were analyzed in the UCSC Stable Isotope
- 102 Laboratory using a CE instruments NC2500 elemental analyzer coupled with Thermo Scientific
- 103 Delta Plus XP iRMS via a Thermo-Scientific Conflo III. All samples are calibrated with VPDB
- 104 (Vienna PeeDee Belemnite) for δ^{13} C and AIR for δ^{15} N against an in-house gelatin standard
- reference material (PUGel). Analytical reproducibility precision is \pm 0.1 % for δ^{13} C and \pm 0.2 %
- 106 for δ^{15} N.
- 107 2.2.2 Grain Size analysis
- 108 Particle size was measured by laser diffraction using Beckman Coulter with Polarization
- 109 Intensity Differential Scatter (PIDS) housed at UCSC. 2 to 5 mg of bulk sediments was powered
- in each sample for measurement. Each sample was performed 2 or 3 replicates to ensure
- 111 reproducibility.
- 112 2.2.3 Clay Assemblages analysis
- 113 Sample preparation follows a slightly modified version of (Kemp et al., 2016). Roughly 5 to 10 g
- 114 of sediment was powdered in a pestle and mortar and then placed in a Calgon (Sodium
- hexametaphosphate) solution on a shaker table for 72 hours. Samples were sorted through a 63
- 116 μm sieve while collecting the fluid with the <63 μm fraction. The collected fluid and suspended
- 117 fine fraction ($< 63 \mu m$) were allowed to settle for a period determined by Stokes' Law to keep <
- 118 2um size clay particles remaining in suspension. The fluid is then decanted and dried in the oven.
- Approximately 150 mg clay of each sample is used to prepared oriented mounts for X-ray
- diffraction (XRD) analysis. A total of 38 clay samples were prepared from the Lodo Formation.
- 121 The sample residues are measured on a Philips 3040/60 X'pert Pro X-ray diffraction instrument
- 122 at UCSC. Clay species are identified based on peak positions and intensities representing each
- 123 clay mineral.
- 124 2.2.4 Leaf wax





125 Sediment extraction, compound isolation, and compound-specific isotope measurements were 126 conducted following Tipple et al., 2011. Briefly, sediments were freeze-dried, powdered (~500 g), and extracted with dichloromethane (DCM): methanol (2:1, v/v) using a Soxhlet extractor. 127 Total lipid extracts were concentrated and then separated by column chromatography using silica 128 gel. Normal-alkanes were further purified from cyclic and branched alkanes using urea adduction 129 130 following (Wakeham and Pease, 2004). Normal-alkane abundances were determined using gas chromatograph (GC) with a flame ionization detector (FID). Isotope analyses were then 131 performed using a GC coupled to an isotope ratio mass spectrometer interfaced with a GC-C III 132 combustion system or a High Temperature Conversion system for δ^{13} C and δ^{2} H analyses, 133 respectively. δ^{13} C and δ^{2} H values are expressed relative to Vienna Pee Dee belemnite (VPDB) 134 and Vienna Standard Mean Ocean Water (VSMOW). Individual n-alkane isotope ratios were 135 corrected to n-alkane reference materials (for δ¹³C, C20, C25, C27, C30, and C38 of known 136 isotopic ratio and for δ^2 H, "Mix A" from Arndt Schimmelmann, Indiana University) analyzed 137 daily at several concentrations. In addition, H₂ reference gas of known isotopic composition was 138 pulsed between sample n-alkane peaks to confirm if normalizations were appropriate. Standard 139 deviations (SD) of n-alkane reference materials was $\pm 0.6\%$ for δ^{13} C and $\pm 6\%$ for δ^{2} H. 140 141 2.2.5 Earth System Models Two different set of climate simulations were used in this paper for (1) comparison with leaf wax 142 proxy data and (2) extreme events analysis. (1) Water isotope-enabled Community Earth System 143 Model version 1.2 (iCESM1.2) simulates changes in climate and water isotopic composition 144 145 during the PETM (Zhu et al., 2020) with a horizontal resolution of 1.9×2.5° in atmosphere and land, and a nominal 1 degree in the ocean and sea ice components. Water isotope capabilities 146 147 have been incorporated into all the components of CESM 1.2 (Brady et al., 2019), which include the Community Atmosphere Model, version 5(CAM5) for the atmosphere, the Parellel Ocean 148 149 Program, version 2(POP2) for the ocean, the Community Land Model, version 4(CLM4) for the 150 land, River Transport Model (RTM) for river flow, and Community Ice Code, version 4 for sea ice. (2) Using the same CESM1.2 framework, high resolution (0.25°) simulations were 151 conducted with forced sea surface temperatures (SSTs) and active atmosphere and land 152 153 components (CAM5, CLM4). RTM was run at 1° resolution, and forced SST were calculated from consistent 2° fully coupled PETM simulations (see details in Rush et al., 2021 and 154





reference therein). The much higher horizontal resolution in the atmosphere enables improved simulation of the extreme events. Hourly, daily (CAM5), and monthly(iCESM1.2) temporal resolution precipitation outputs from both sets of climate simulations were utilized in this paper, with 100 years taken from the equilibrated iCESM1.2 simulations, and 15 years from the forced SST high resolution CAM5 simulations.

3 Results

3.1 Carbon isotopes

A carbon isotope excursion is present in both bulk organic and carbonate based δ^{13} C records across the P-E boundary (Fig. 2a), marking the PETM onset of the Lodo section(John et al., 2008). The terrestrial leaf wax n-alkane record captures the carbon isotope excursion (CIE) with a pattern that roughly parallels the other records. The magnitude of the δ^{13} C_{n-alkane} change is roughly 4 ‰ (average of n-C₂₇, n-C₂₉, n-C₃₁) at the onset, followed by a gradual recovery that is truncated marking the top of the PETM body (Fig. 3b).

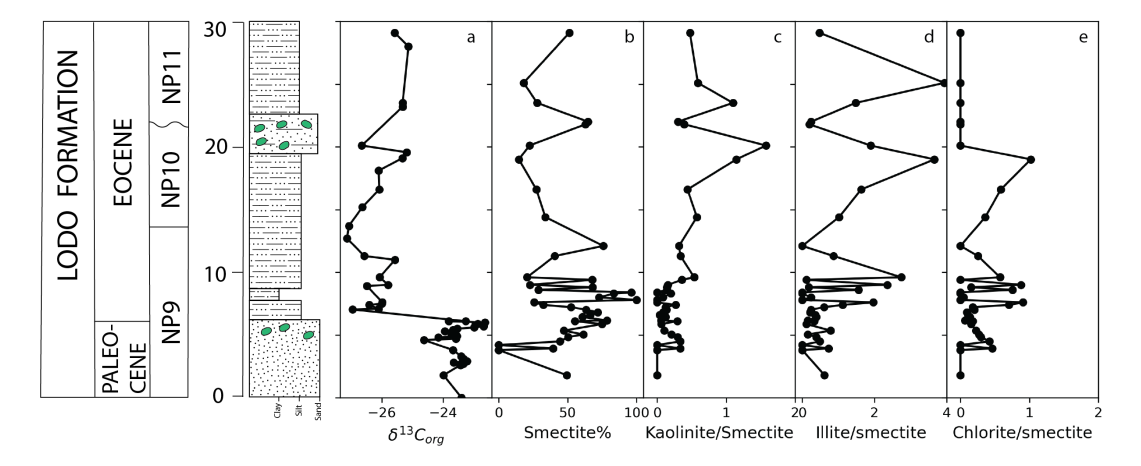


Figure 2. Integrated C isotope and clay assemblage records of Lodo Fm in the Lodo Gulch of central California (a) bulk organic carbon isotope, (b,c,d,e) clay assemblage ratios.





3.2 Hydrogen isotopes

The leaf wax $\delta^2 H_{\text{n-alkane}}$ values decrease by 25% just prior to the CIE onset followed by a slight enrichment of in the main body PETM (Fig. 3c). The relatively invariable $\delta^2 H_{\text{n-alkane}}$ through the PETM is punctuated with one or two brief intervals of more negative values.

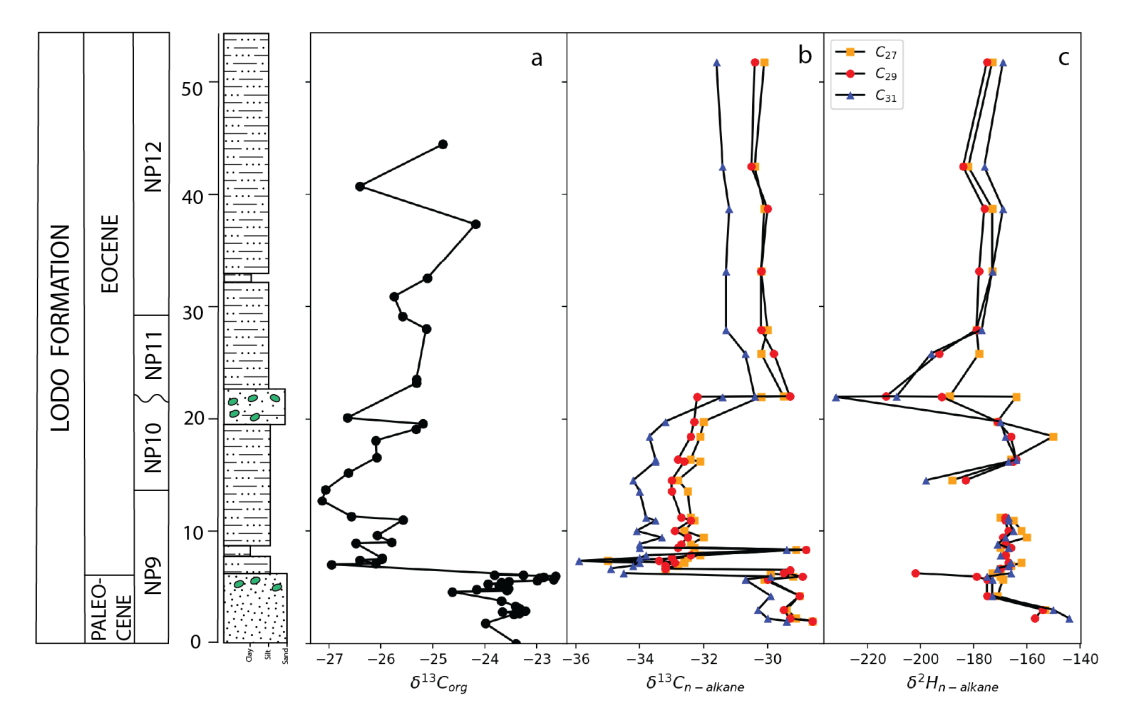


Figure 3. Marine δ^{13} C and terrestrial higher plant leaf wax n-alkane δ^{13} C and δ^{2} H records. (a) bulk organic carbon isotope record of Lodo Fm. (b,c) leaf wax compound specific carbon/hydrogen isotope records in n-C₂₇(yellow), n-C₂₉(red), n-C₃₁(blue).

3.3 Clay Assemblage and grain Size

Clay assemblage data (Fig. 2) shows smectite dominated in the Lodo Formation during PETM, along with increasing illlite/smectite and chlorite/smectite ratios. The lower Lodo Formation, with relative coarse sandy size, shows slight spikes of kaolinite associated with other minerals. Grain size, largely silt and clay, shows a distinct shift toward finer fractions (i.e., clay) with the onset of the CIE (Fig. S1).





 3.4 Earth system model simulations

Precipitation output from two earth system models: isotope enabled iCESM1.2 under enhanced greenhouse gas simulations (1x,3x,6x,9x pCO₂ pre-industrial) and high-resolution CAM5 models (daily precipitation over 15 years), were analyzed. For this study we used 3x to 6x pCO₂ forcing that best replicate the observed Δ SST from pre-PETM to PETM(Zhu et al., 2020). Overall, monthly precipitation for the study region decreases during the PETM in both simulations but with a slight increase in the summer (Fig. 4,5). CAM5 output shows a modest decrease in mean annual precipitation with significant seasonal shifts during PETM (Fig. 5a). Seasonal changes of monthly averaged δ ¹⁸O and δ ²H from mean monthly precipitation (MAP) in iCESM1.2 of central California are consistent with CAM5. On average the δ ²H increases by ca. 10 % from pre-PETM to PETM, especially in the winter/spring, with a smaller shift in summer/fall (Fig 4. a,b,c). The Extreme value index (ξ), a representation of the distribution of exceedance right tail (supplemental information), shows a small but statistically robust increase in wet extremes of winter (DJF) with a significant increase in summer (JJA) wet exceedances during the PETM in the precipitation output from CAM5 simulations (Fig. 5b).

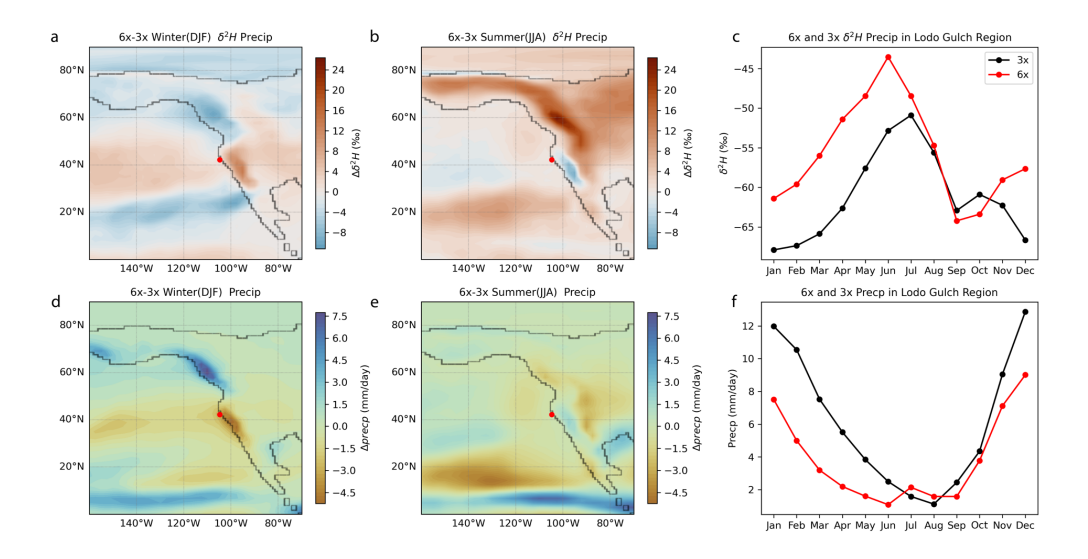


Figure 4. Water isotope-enable iCESM1.2 model output (Zhu et al., 2020) of monthly hydrogen isotope record of meteoric precipitation under different pCO₂ forcing to pre-industry (3x in black





represents pre-PETM, 6x in red represents PETM) in east Pacific coast (red spot represents the Lodo Gulch study site). The iCESM1.2 simulations used the DeepMIP boundary conditions (Lunt et al., 2017). Difference in winter (a) and summer (b) hydrogen isotope composition between pre-PETM(3x) and PETM(6x). (c) Annual seasonal cycle of hydrogen isotope composition of precipitation in Lodo Gulch region. Difference in winter(d) and summer(e) precipitation amount between pre-PETM(3x) and PETM(6x) in east Pacific coast. (f) Annual seasonal cycle of precipitation amount in Lodo Gulch region. Site values of Lodo Gulch region are calculated by area-weighted average over 4° x 4° box around study site.

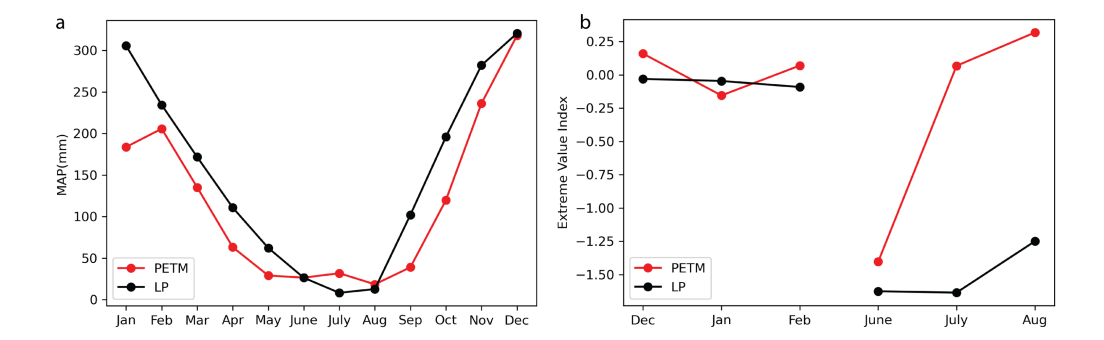


Figure 5. (a) High resolution CAM5 model output of mean monthly precipitation over 15 model years in central coastal California regions during pre-PETM (Late Paleocene/LP) under low pCO_2 (680 ppmv) and PETM under high pCO_2 (1590ppmv). (b) Extreme value index (ξ) results of mean monthly precipitation in winter versus summer of central coastal California region.

4 Discussion

Independent proxies (i.e, sediment flux, clay assemblages, and water isotopes (²H/¹H or ¹⁸O/¹⁶O), though each has limitations, collectively can contribute toward a general picture of how the mode of precipitation changed (i.e., wetter or dryer, and/or greater seasonality or extremes). For central California, model simulations of the PETM with low and high resolutions exhibit an overall decrease in mean annual precipitation (Fig. 4,5). For a mountainous coastal environment (Fig. 1), siliciclastic sedimentation rates should be highly susceptible to hydrologic changes among other factors. In addition to relief and lithology, the seasonality of precipitation and vegetation cover would be major controls on erosion and siliciclastic sediment fluxes. However, constraining sedimentation rates in shelf sections is challenging given the limitations of





237 chronostratigraphy in such facies. As such, we rely largely on biostratigraphic constraints with 238 carbon isotope stratigraphy as the CIE is well captured in both organic and inorganic (calcite) fossil materials in Lodo (John et al., 2008). This expanded CIE interval indicates higher 239 sedimentation rates during the PETM (John et al., 2008). Sedimentation rates on the continental 240 shelf margin are highly sensitive to terrestrial sediment discharge and relative sea-level change. 241 Assuming the latter was relatively static or rising (Sluijs et al., 2008), the higher sedimentation 242 rates suggest increasing sediment supply from river runoff to the continental margin, reflecting a 243 mode shift in regional hydroclimate. 244 245 4.1 Hydroclimate response from clay mineralogy 246 Clay assemblages in nearshore settings can reflect physical and chemical weathering changes as 247 influenced by regional climate change. Indeed, an increase in the relative abundance of kaolinite 248 fluxes has been widely observed across the CIE onset in many PETM sections from mid to high 249 250 latitudes(Tateo, 2020; Gibson et al., 2000) and interpreted as evidence of a major mode shift in local hydroclimates. In contrast, the clay mineralogy (Fig. 3) for the Lodo Formation is 251 dominated mainly by smectite at the onset of the PETM, consistent with seasonal wet/dry cycles 252 253 under warm conditions (Gibson et al., 2000). A subtle increase in the kaolinite/smectite hints slightly enhanced humidity, possibly related to enhanced seasonally subtropical 254 255 conditions(Foreman, 2014). Such inferences of hydroclimate changes in the context of coastal deposition are complicated by fluvial runoff conditions (i.e., provenance, discharge, sediment 256 257 influx) and precipitation (i.e., seasonal vs mean annual). Skewed grain size distribution of clay 258 sediments coinciding with illite/kaolinite peaks (Fig. S1) indicates higher fluvial velocity and increased erosion as observed in other locations(Chen et al., 2018; Foreman et al., 2012; 259 Foreman, 2014). The lower Lodo Formation, with relative coarse sandy size distribution 260 261 preceding the PETM, shows a slight pulse of kaolinite associated with other minerals, possibly indicating an early change of hydrological condition in the latest Paleocene before the PETM as 262 263 observed elsewhere (Rush et al., 2021). The CIE onset likely represents a transient response to warming-induced hydroclimate changes, whereas the pre-PETM shift as well as minor variations 264 265 post-CIE onset are likely orbitally forced (Kiehl et al., 2018).

4.2 Hydroclimate response from earth system simulations





267 In all model simulations forced with higher pCO2 (e.g., 3x to 6x pre-industrial), the hydrological 268 cycle during PETM intensifies as manifested by increases in global mean precipitation and meridional vapor transport (Kiehl and Shields, 2013; Kiehl et al., 2018; Carmichael et al., 2016; 269 Zhu et al., 2020). Regionally however, the magnitude and even the sign of precipitation change 270 can differ considerably from global means. This is most evident in the latest low and high-271 272 resolution model simulations of the PETM. For central California, the simulations yield modest changes in mean annual precipitation but significant seasonal shifts with a notable decline in 273 winter precipitation and a slight increase in summer (Fig. 4). This pattern is produced by both the 274 water isotope enabled iCESM1.2 and the higher resolution CAM5 with an overall shift into 275 lower amplitude seasonal cycles as a drier winter/spring and a slightly wetter summer (Fig. 4, 5). 276 This seasonal wet-dry shift appears to be driven in part by a pronounced northward shift of 277 atmospheric rivers (ARs) in winter along the Pacific coast(Shields et al., 2021). Given the ARs 278 delivering the majority of winter precipitation to the mid-latitude Pacific coast, less frequent AR 279 280 occurrences would result in relatively drier winters during PETM. Moreover, the extreme value index (ξ) shows a small but statistically robust increase winter (DF) wet extremes with a 281 282 significant increase in the probability of summer (JJA) wet exceedance during PETM (Fig. 5b). 283 Although AR related coastal winter storms reduced in frequency (Shields et al., 2021), summer precipitation increased in intensity thus potentially enhancing individual extremes in this region, 284 285 possibly related to an increase in summer tropical storm activity along the Pacific coast during PETM (Fig. S4). 286 4.3 ²H/¹H composition of leaf waxes. 287 Terrestrial archives exhibit considerable evidence of environmental response to intensified 288 hydrological cycle during the PETM (McInerney and Wing, 2011). In western North America, 289 290 plant fossils show widely expansion (up to 40°N) of tropical rainforest during the PETM along 291 the east Pacific in mid-latitude(Willis, K.J, McElwain, 2002; Korasidis et al., 2022). Terrestrial higher plant hydrogen isotope composition (i.e., $\delta^2 H_{n-alkane}$) provide evidence for regional mode 292 shifts of precipitation (Handley et al., 2008, 2011; Jaramillo et al., 2010; Pagani et al., 2006; 293 Tipple et al., 2011). Generally, δ^2 H significantly increases in most of these records as expected 294 295 with warming, but regionally, notable similarities and differences existed. In subtropical/midlatitude regions, δ^2 H increases prior to the PETM followed by a large negative excursion (ca 296 297 ~20‰) across the onset of PETM (Handley et al., 2008, 2011; Jaramillo et al., 2010; Tipple et





298 al., 2011). In sharp contrast, high latitudes $\delta^2 H_{\text{n-alkane}}$ show a positive excursion of 55% at CIE 299 onset during PETM, consistent with a reduced meridional temperature gradient and decreasing isotope distillation during vapor transport (Pagani et al., 2006). However, the Lodo $\delta^2 H_{\text{n-alkane}}$ 300 displays a comparatively muted response, initially decreasing by 25% just prior to the CIE onset 301 followed by a slight ²H enrichment in the main body PETM followed by several shifts toward 302 303 more negative values (Fig. 3c). The shift to more negative $\delta^2 H_{n-alkane}$ values prior to the onset of 304 CIE in Lodo likely represents background variability related to orbital forcing. Inferring and comparing the hydroclimate response from leaf water $\delta^2 H$ at any location can be 305 complicated. Hydrogen isotope fractionation in plants is tightly related to photosynthetic 306 pathways, source water availability, and atmospheric humidity (Sachse et al., 2012; Tipple et al., 307 308 2015). Along the west coast of North America, no detailed records of vegetation response have been generated for the PETM. Lack of knowledge about vegetation changes limits our ability to 309 compute rainwater δ^2 H. Further, under higher weathering rates during the PETM, deep 310 311 weathering of Paleocene n-alkanes (Tipple et al., 2011) would possibly dampen of isotopic nalkane signals deposited at Lodo. Nevertheless, if we assume the $\delta^2 H_{n-alkane}$ record reflects only 312 313 on changes in source water, the observed modest change of $\delta^2 H_{\text{n-alkane}}$ values at Lodo could be interpreted in several ways with respect to T-related changes on isotope fractionation offset by 314 changes in dominant season of precipitation, and/or vapor sources and distance of transport. For 315 example, a shift in precipitation seasonally between winter and late summer/fall could offset the 316 317 effects of warming assuming a shift from a proximal (north or central Pacific) to a more distal (Gulf of Mexico) source of vapor (Hu and Dominguez, 2015). At ground level, stronger 318 evapotranspiration during biosynthesis can isotopically be offset by external water source 319 availability (i.e. seasonal precipitation). Local/regional ground water table variations caused by 320 321 hydrological change would also affect the source water-use efficiency of plants since surface 322 water tends to be more depleted in some perennial species after intense storms in the 323 groundwater (Hou et al., 2008; Krishnan et al., 2014). Hydrogen isotope fractionation in plants can also be biased by seasonal shift in regional vegetation growth regime. For example, leaf wax 324 325 lipids from terrestrial plants usually record hydrological conditions earlier in the season rather than fully integrating the entire growing season (Hou et al., 2008; Tipple et al., 2013). Finally, 326 episodic extremes in precipitation may dominate the hydrogen isotopic composition of the leaf 327 328 wax (Krishnan et al., 2014). If most soil water from extreme events during the growth season, the





329 Lodo $\delta^2 H_{\text{n-alkane}}$ changes might reflect a combination effect of intensified seasonal storms with 330 more ²H-depleted precipitation offset by warming induced ²H-enrichment in leaf water. 331 In iCESM1.2 simulations with increasing pCO_2 (i.e., 3x to 6x pre-industry) and SST, the 332 seasonal shifts in δ^2 H of mean monthly precipitation from pre-PETM to PETM is significant. 333 334 Regional $\delta^2 H_{\text{precp}}$ increases by 10% during wet winter while decreasing by ~1 to 5% during late 335 summer/fall in central California (Fig. 4). To estimate how this seasonal change of $\delta^2 H_{precp}$ and 336 precipitation amount influences leaf water δ^2 H, we apply a leaf wax proxy model (supplemental 337 information) which computes the combined effects of changes in seasonal precipitation and growing season length. The model shows leaf water δ^2 H enriched ca. 4 to 7% from pre-PETM to 338 339 PETM consistent with δ^2 H_{n-alkane} proxy record in Lodo section. Therefore, this relative muted 340 leaf wax $\delta^2 H_{n-alkane}$ response can be potentially explained by a seasonal shift of heavy 341 precipitation events. Alternatively, the change in leaf water δ^2 H may also reflect source water shift of a mixing endmember between proximal and distal sources of water in the coast (Romero 342 343 and Feakins, 2011). For example, with a summer shift of source water from the Pacific to subtropics (i.e., summer monsoons), the effect of increasing distance and distillation would 344 345 isotopically deplete vapor (Hu and Dominguez, 2015), thus offsetting the temperature related enrichment of local δ^2 H_{precip}. Infrequent but high intensity tropical cyclones-induced heavy 346 rainfall in the summer in mid-Pacific during PETM (Kiehl et al., 2021) can also bring the 347 precipitation more depleted in hydrogen isotope (i.e., a more negative $\delta^2 H$). 348 349 Finally, a related record that might indirectly reflect on precipitation amount (i.e., atmospheric 350 humidity) is the n-alkane δ^{13} C and magnitude of the CIE. Recalcitrant higher plants leaf wax 351 carbon isotope ratios of long-chain n-alkane (n>25 with odd-over-even preference) reflect 352 353 mainly carbon source (Diefendorf et al., 2010). However, photosynthetic carbon isotope fractionation (Δ_p) is sensitive to atmospheric pCO₂ variations, generally increase with rising 354 355 concentrations assuming a constant photosynthetic fractionation factor and humidity (Diefendorf et al., 2010). The $\delta^{13}C_{n-alkane}$ of Lodo section displays a sharp negative shift of ca. 4 ‰ (average 356 of n-C₂₇, n-C₂₉, n-C₃₁) across the onset of CIE (Fig. 3b), which is consistent with global mean 357 358 atmospheric CIE (Sluijs and Dickens, 2012) but generally smaller than observed in other leaf wax records (Handley et al., 2008, 2011; Jaramillo et al., 2010; Pagani et al., 2006; Tipple et al., 359







360 2011). The smaller δ^{13} C_{n-alkane} CIE recorded in Lodo could reflect on reduction in local humidity 361 which preferentially tends to reduce the magnitude of Δ_p during photosynthetic carbon fixation. 362 **5 Conclusion** 363 With PETM greenhouse gas forcing (~56 Ma), climate simulations show an overall decrease in 364 365 winter precipitation along the central California margin due in part to a reduction in AR frequency(Shields et al., 2021), whereas summer precipitation increases slightly. This is 366 generally consistent with the observations from Lodo Gulch Section based on various 367 sedimentological and geochemical records, and thus would support a modest reduction in 368 precipitation (i.e. MAP) along with the possibility of an increase magnitude of extreme 369 370 precipitation events during the PETM. In this regard, the observed hydroclimate response during the PETM as simulated in climate models in response to a doubling (or more) of CO₂ could serve 371 as a past analog for potential hydroclimate changes in California. 372 373 374 Data availability. Data will be available via the PANGAEA repository. 375 376 377 Author contribution. JCZ conceived the project idea, acquired funding and provided overall 378 supervision. XZ, BJT, WDR, JBN conducted experiments and analyzed the results. JZ, CAS provide technical expertise in model simulations. All authors contributed to the review and 379 editing of the manuscript. 380 381 Competing interests. The authors declare that they have no conflict of interest. 382 383 384 Acknowledgements. 385 Funding for this project has been provided by National Science Foundation No. OCE 2103513. All compound specific isotope analyses were performed at the Yale Institute for Biospheric 386 Studies-Earth Systems Center for Stable Isotopic Studies that was supported by National Science 387 Foundation Grant EAR 0628358 and OCE 0902993. The CESM project is supported primarily 388 by the National Science Foundation (NSF). This material is based upon work supported by the 389 National Center for Atmospheric Research, which is a major facility sponsored by the NSF under 390 Cooperative Agreement No. 1852977. 391 392





394 Reference:

- 395 Abell, J. T., Winckler, G., Anderson, R. F., and Herbert, T. D.: Poleward and weakened westerlies
- 396 during Pliocene warmth, Nature, 589, 70–75, https://doi.org/10.1038/s41586-020-03062-1, 2021.
- 397 Brabb, E. E.: Studies in Tertiary stratigraphy of the California Coast Ranges., US Geological
- 398 Survey Professional Paper, 1213, 1983.
- 399 Brady, E., Stevenson, S., Bailey, D., Liu, Z., Noone, D., Nusbaumer, J., Otto-Bliesner, B. L., Tabor,
- 400 C., Tomas, R., Wong, T., Zhang, J., and Zhu, J.: The Connected Isotopic Water Cycle in the
- 401 Community Earth System Model Version 1, J Adv Model Earth Syst, 11, 2547–2566,
- 402 https://doi.org/10.1029/2019MS001663, 2019.
- 403 Büntgen, U., Urban, O., Krusic, P. J., Rybníček, M., Kolář, T., Kyncl, T., Ač, A., Koňasová, E.,
- Čáslavský, J., Esper, J., Wagner, S., Saurer, M., Tegel, W., Dobrovolný, P., Cherubini, P.,
- 405 Reinig, F., and Trnka, M.: Recent European drought extremes beyond Common Era background
- 406 variability, Nat Geosci, 14, 190–196, https://doi.org/10.1038/s41561-021-00698-0, 2021.
- 407 Carmichael, M. J., Lunt, D. J., Huber, M., Heinemann, M., Kiehl, J., LeGrande, A., Loptson, C. A.,
- 408 Roberts, C. D., Sagoo, N., Shields, C., Valdes, P. J., Winguth, A., Winguth, C., and Pancost, R.
- 409 D.: A model-model and data-model comparison for the early Eocene hydrological cycle, Climate
- 410 of the Past, 12, 455–481, https://doi.org/10.5194/CP-12-455-2016, 2016.
- 411 Carmichael, M. J., Inglis, G. N., Badger, M. P. S., Naafs, B. D. A., Behrooz, L., Remmelzwaal, S.,
- 412 Monteiro, F. M., Rohrssen, M., Farnsworth, A., Buss, H. L., Dickson, A. J., Valdes, P. J., Lunt,
- 413 D. J., and Pancost, R. D.: Hydrological and associated biogeochemical consequences of rapid
- 414 global warming during the Paleocene-Eocene Thermal Maximum,
- 415 https://doi.org/10.1016/j.gloplacha.2017.07.014, 1 October 2017.
- 416 Chen, C., Guerit, L., Foreman, B. Z., Hassenruck-Gudipati, H. J., Adatte, T., Honegger, L., Perret,
- 417 M., Sluijs, A., and Castelltort, S.: Estimating regional flood discharge during Palaeocene-Eocene
- 418 global warming, Sci Rep, 8, 1–8, https://doi.org/10.1038/s41598-018-31076-3, 2018.
- 419 Diefendorf, A. F., Mueller, K. E., Wing, S. L., Koch, P. L., and Freeman, K. H.: Global patterns in
- 420 leaf 13C discrimination and implications for studies of past and future climate, Proc Natl Acad
- 421 Sci U S A, 107, 5738–5743, https://doi.org/10.1073/pnas.0910513107, 2010.
- 422 Douville, H., Raghavan, K., Renwick, J., and Allan, R.: Water Cycle Changes, Intergovernmental
- 423 Panel on Climate Change 2021 The Physical Science Basis, 1055–1210,
- 424 https://doi.org/10.1017/9781009157896.010, 2021.
- 425 Foreman, B. Z.: Climate-driven generation of a fluvial sheet sand body at the Paleocene–Eocene
- boundary in north-west Wyoming (USA), Basin Research, 26, 225–241,
- 427 https://doi.org/10.1111/BRE.12027, 2014.
- 428 Foreman, B. Z., Heller, P. L., and Clementz, M. T.: Fluvial response to abrupt global warming at
- 429 the Palaeocene/Eocene boundary, Nature 2012 491:7422, 491, 92–95,
- 430 https://doi.org/10.1038/nature11513, 2012.
- 431 Gibson, T. G., Bybell, L. M., and Mason, D. B.: Stratigraphic and climatic implications of clay
- 432 mineral changes around the Paleocene/Eocene boundary of the northeastern US margin,
- 433 Sediment Geol, 134, 65–92, https://doi.org/10.1016/S0037-0738(00)00014-2, 2000.
- 434 Handley, L., Pearson, P. N., McMillan, I. K., and Pancost, R. D.: Large terrestrial and marine
- 435 carbon and hydrogen isotope excursions in a new Paleocene/Eocene boundary section from
- 436 Tanzania, Earth Planet Sci Lett, 275, 17–25, https://doi.org/10.1016/j.epsl.2008.07.030, 2008.





- 437 Handley, L., Crouch, E. M., and Pancost, R. D.: A New Zealand record of sea level rise and
- 438 environmental change during the Paleocene-Eocene Thermal Maximum, Palaeogeogr
- 439 Palaeoclimatol Palaeoecol, 305, 185–200, https://doi.org/10.1016/j.palaeo.2011.03.001, 2011.
- 440 Handley, L., O'Halloran, A., Pearson, P. N., Hawkins, E., Nicholas, C. J., Schouten, S., McMillan,
- 441 I. K., and Pancost, R. D.: Changes in the hydrological cycle in tropical East Africa during the
- Paleocene-Eocene Thermal Maximum, Palaeogeogr Palaeoclimatol Palaeoecol, 329–330, 10–21,
- 443 https://doi.org/10.1016/j.palaeo.2012.02.002, 2012.
- 444 Held, I. M. and Soden, B. J.: Robust Responses of the Hydrological Cycle to Global Warming, J
- 445 Clim, 19, 5686–5699, https://doi.org/10.1175/JCLI3990.1, 2006.
- 446 Hou, J., D'Andrea, W. J., and Huang, Y.: Can sedimentary leaf waxes record D/H ratios of
- 447 continental precipitation? Field, model, and experimental assessments, Geochim Cosmochim
- 448 Acta, 72, 3503–3517, https://doi.org/10.1016/j.gca.2008.04.030, 2008.
- 449 Hu, H. and Dominguez, F.: Evaluation of Oceanic and Terrestrial Sources of Moisture for the North
- 450 American Monsoon Using Numerical Models and Precipitation Stable Isotopes, J
- 451 Hydrometeorol, 16, 19–35, https://doi.org/10.1175/JHM-D-14-0073.1, 2015.
- 452 Jaramillo, C., Ochoa, D., Contreras, L., Pagani, M., Carvajal-Ortiz, H., Pratt, L. M., Krishnan, S.,
- 453 Cardona, A., Romero, M., Quiroz, L., Rodriguez, G., Rueda, M. J., De La Parra, F., Morón, S.,
- 454 Green, W., Bayona, G., Montes, C., Quintero, O., Ramirez, R., Mora, G., Schouten, S.,
- Bermudez, H., Navarrete, R., Parra, F., Alvarán, M., Osorno, J., Crowley, J. L., Valencia, V., and
- 456 Vervoort, J.: Effects of rapid global warming at the paleocene-eocene boundary on neotropical
- 457 vegetation, Science (1979), 330, 957–961, https://doi.org/10.1126/science.1193833, 2010.
- 458 John, C. M., Bohaty, S. M., Zachos, J. C., Sluijs, A., Gibbs, S., Brinkhuis, H., and Bralower, T. J.:
- 459 North American continental margin records of the Paleocene-Eocene thermal maximum:
- 460 Implications for global carbon and hydrological cycling, Paleoceanography, 23,
- 461 https://doi.org/10.1029/2007PA001465, 2008.
- 462 Kemp, S. J., Ellis, M. A., Mounteney, I., and Kender, S.: Palaeoclimatic implications of high-
- 463 resolution clay mineral assemblages preceding and across the onset of the Palaeocene–Eocene
- Thermal Maximum, North Sea Basin, Clay Miner, 51, 793–813,
- 465 https://doi.org/10.1180/CLAYMIN.2016.051.5.08, 2016.
- 466 Kiehl, J. T. and Shields, C. A.: Sensitivity of the palaeocene-eocene thermal maximum climate to
- cloud properties, Philosophical Transactions of the Royal Society A: Mathematical, Physical and
- 468 Engineering Sciences, 371, https://doi.org/10.1098/rsta.2013.0093, 2013.
- 469 Kiehl, J. T., Shields, C. A., Snyder, M. A., Zachos, J. C., and Rothstein, M.: Greenhouse- and
- 470 orbital-forced climate extremes during the early Eocene, Philosophical Transactions of the Royal
- 471 Society A: Mathematical, Physical and Engineering Sciences, 376,
- 472 https://doi.org/10.1098/RSTA.2017.0085, 2018.
- 473 Kiehl, J. T., Zarzycki, C. M., Shields, C. A., and Rothstein, M. V.: Simulated changes to tropical
- 474 cyclones across the Paleocene-Eocene Thermal Maximum (PETM) boundary, Palaeogeogr
- 475 Palaeoclimatol Palaeoecol, 572, 110421, https://doi.org/10.1016/J.PALAEO.2021.110421, 2021.
- 476 Korasidis, V. A., Wing, S. L., Shields, C. A., and Kiehl, J. T.: Global Changes in Terrestrial
- 477 Vegetation and Continental Climate During the Paleocene-Eocene Thermal Maximum,
- 478 Paleoceanogr Paleoclimatol, 37, https://doi.org/10.1029/2021PA004325, 2022.
- 479 Kozdon, R., Penman, D. E., Kelly, D. C., Zachos, J. C., Fournelle, J. H., and Valley, J. W.:
- Enhanced Poleward Flux of Atmospheric Moisture to the Weddell Sea Region (ODP Site 690)
- During the Paleocene-Eocene Thermal Maximum, Paleoceanogr Paleoclimatol, 35, 1–14,
- 482 https://doi.org/10.1029/2019pa003811, 2020.

© Author(s) 2023. CC BY 4.0 License.





- 483 Kraus, M. J. and Riggins, S.: Transient drying during the Paleocene-Eocene Thermal Maximum
- 484 (PETM): Analysis of paleosols in the bighorn basin, Wyoming, Palaeogeogr Palaeoclimatol
- 485 Palaeoecol, 245, 444–461, https://doi.org/10.1016/j.palaeo.2006.09.011, 2007.
- 486 Krishnan, S., Pagani, M., Huber, M., and Sluijs, A.: High latitude hydrological changes during the
- 487 Eocene Thermal Maximum 2, Earth Planet Sci Lett, 404, 167–177,
- 488 https://doi.org/10.1016/j.epsl.2014.07.029, 2014.
- 489 Liu, B., Yan, Y., Zhu, C., Ma, S., and Li, J.: Record-Breaking Meiyu Rainfall Around the Yangtze
- 490 River in 2020 Regulated by the Subseasonal Phase Transition of the North Atlantic Oscillation,
- 491 Geophys Res Lett, 47, https://doi.org/10.1029/2020GL090342, 2020.
- 492 Massoud, E. C., Espinoza, V., Guan, B., and Waliser, D. E.: Global Climate Model Ensemble
- 493 Approaches for Future Projections of Atmospheric Rivers, Earths Future, 7, 1136–1151,
- 494 https://doi.org/10.1029/2019EF001249, 2019.
- 495 McInerney, F. A. and Wing, S. L.: The Paleocene-Eocene Thermal Maximum: A Perturbation of
- 496 Carbon Cycle, Climate, and Biosphere with Implications for the Future, Annu Rev Earth Planet
- 497 Sci, 39, 489–516, https://doi.org/10.1146/annurev-earth-040610-133431, 2011.
- 498 Nicolo, M. J., Dickens, G. R., and Hollis, C. J.: South Pacific intermediate water oxygen depletion
- 499 at the onset of the Paleocene-Eocene thermal maximum as depicted in New Zealand margin
- 500 sections, Paleoceanography, 25, 1–12, https://doi.org/10.1029/2009PA001904, 2010.
- 501 Pagani, M., Pedentchouk, N., Huber, M., Sluijs, A., Schouten, S., Brinkhuis, H., Damsté, J. S. S.,
- 502 Dickens, G. R., Backman, J., Clemens, S., Cronin, T., Eynaud, F., Gattacceca, J., Jakobsson, M.,
- 503 Jordan, R., Kaminski, M., King, J., Koc, N., Martinez, N. C., McInroy, D., Moore, T. C.,
- 504 O'Regan, M., Onodera, J., Pälike, H., Rea, B., Rio, D., Sakamoto, T., Smith, D. C., St John, K.
- 505 E. K., Suto, I., Suzuki, N., Takahashi, K., Watanabe, M., and Yamamoto, M.: Arctic hydrology
- during global warming at the Palaeocene/Eocene thermal maximum, Nature, 442, 671–675,
- 507 https://doi.org/10.1038/nature05043, 2006.
- 508 Polade, S. D., Gershunov, A., Cayan, D. R., Dettinger, M. D., and Pierce, D. W.: Precipitation in a
- 509 warming world: Assessing projected hydro-climate changes in California and other
- 510 Mediterranean climate regions OPEN, Sci Rep, 7, https://doi.org/10.1038/s41598-017-11285-y,
- 511 2017.
- 512 Risser, M. D. and Wehner, M. F.: Attributable Human-Induced Changes in the Likelihood and
- 513 Magnitude of the Observed Extreme Precipitation during Hurricane Harvey, Geophys Res Lett,
- 514 44, 12,457-12,464, https://doi.org/10.1002/2017GL075888, 2017.
- 515 Romero, I. C. and Feakins, S. J.: Spatial gradients in plant leaf wax D/H across a coastal salt marsh
- 516 in southern California, Org Geochem, 42, 618–629,
- 517 https://doi.org/10.1016/J.ORGGEOCHEM.2011.04.001, 2011.
- 518 Rush, W. D., Kiehl, J. T., Shields, C. A., and Zachos, J. C.: Increased frequency of extreme
- 519 precipitation events in the North Atlantic during the PETM: Observations and theory,
- 520 Palaeogeogr Palaeoclimatol Palaeoecol, 568, https://doi.org/10.1016/j.palaeo.2021.110289,
- 521 2021.
- 522 Sachse, D., Billault, I., Bowen, G. J., Chikaraishi, Y., Dawson, T. E., Feakins, S. J., Freeman, K. H.,
- 523 Magill, C. R., McInerney, F. A., van der Meer, M. T. J., Polissar, P., Robins, R. J., Sachs, J. P.,
- 524 Schmidt, H.-L., Sessions, A. L., White, J. W. C., West, J. B., and Kahmen, A.: Molecular
- 525 Paleohydrology: Interpreting the Hydrogen-Isotopic Composition of Lipid Biomarkers from
- 526 Photosynthesizing Organisms, Annu Rev Earth Planet Sci, 40, 221–249,
- 527 https://doi.org/10.1146/annurev-earth-042711-105535, 2012.





- 528 Schmitz, B. and Pujalte, V.: Sea-level, humidity, and land-erosion records across the initial Eocene
- thermal maximum from a continental-marine transect in northern Spain, Geology, 31, 689–692,
- 530 https://doi.org/10.1130/G19527.1, 2003.
- 531 Self-Trail, J. M., Robinson, M. M., Bralower, T. J., Sessa, J. A., Hajek, E. A., Kump, L. R.,
- Trampush, S. M., Willard, D. A., Edwards, L. E., Powars, D. S., and Wandless, G. A.: Shallow
- 533 marine response to global climate change during the Paleocene-Eocene Thermal Maximum,
- 534 Salisbury Embayment, USA, Paleoceanography, 32, 710–728,
- 535 https://doi.org/10.1002/2017PA003096, 2017.
- 536 Shields, C. A. and Kiehl, J. T.: Atmospheric river landfall-latitude changes in future climate
- 537 simulations, Geophys Res Lett, 43, 8775–8782, https://doi.org/10.1002/2016GL070470, 2016.
- 538 Shields, C. A., Kiehl, J. T., Rush, W., Rothstein, M., and Snyder, M. A.: Atmospheric rivers in
- 539 high-resolution simulations of the Paleocene Eocene Thermal Maximum (PETM), Palaeogeogr
- 540 Palaeoclimatol Palaeoecol, 567, https://doi.org/10.1016/j.palaeo.2021.110293, 2021.
- 541 Simon Wang, S. Y., Yoon, J. H., Becker, E., and Gillies, R.: California from drought to deluge,
- 542 Nature Climate Change 2017 7:7, 7, 465–468, https://doi.org/10.1038/nclimate3330, 2017.
- 543 Slotnick, B. S., Dickens, G. R., Nicolo, M. J., Hollis, C. J., Crampton, J. S., Zachos, J. C., and
- 544 Sluijs, A.: Large-amplitude variations in carbon cycling and terrestrial weathering during the
- 545 latest Paleocene and earliest Eocene: The record at Mead Stream, New Zealand, Journal of
- 546 Geology, 120, 487–505, https://doi.org/10.1086/666743, 2012.
- 547 Sluijs, A. and Brinkhuis, H.: A dynamic climate and ecosystem state during the Paleocene-Eocene
- 548 Thermal Maximum: Inferences from dinoflagellate cyst assemblages on the New Jersey Shelf,
- Biogeosciences, 6, 1755–1781, https://doi.org/10.5194/bg-6-1755-2009, 2009.
- 550 Sluijs, A. and Dickens, G. R.: Assessing offsets between the δ13C of sedimentary components and
- 551 the global exogenic carbon pool across early Paleogene carbon cycle perturbations, Global
- 552 Biogeochem Cycles, 26, https://doi.org/10.1029/2011GB004224, 2012.
- 553 Sluijs, A., Brinkhuis, H., Crouch, E. M., John, C. M., Handley, L., Munsterman, D., Bohaty, S. M.,
- Zachos, J. C., Reichart, G. J., Schouten, S., Pancost, R. D., Damsté, J. S. S., Welters, N. L. D.,
- 555 Lotter, A. F., and Dickens, G. R.: Eustatic variations during the Paleocene-Eocene greenhouse
- world, Paleoceanography, 23, https://doi.org/10.1029/2008PA001615, 2008.
- 557 Smith, F. A., Wing, S. L., and Freeman, K. H.: Magnitude of the carbon isotope excursion at the
- 558 Paleocene-Eocene thermal maximum: The role of plant community change, Earth Planet Sci
- 559 Lett, 262, 50–65, https://doi.org/10.1016/j.epsl.2007.07.021, 2007.
- 560 Stassen, P., Thomas, E., and Speijer, R. P.: The progression of environmental changes during the
- 561 onset of the Paleocene-Eocene thermal maximum (New Jersey coastal plain), Austrian Journal of
- 562 Earth Sciences, 105, 169–178, 2012.
- 563 Stevenson, S., Coats, S., Touma, D., Cole, J., Lehner, F., Fasullo, J., and Otto-Bliesner, B.: Twenty-
- first century hydroclimate: A continually changing baseline, with more frequent extremes,
- 565 PNAS, 119, https://doi.org/10.1073/pnas, 2022.
- 566 Swain, D. L., Langenbrunner, B., Neelin, J. D., and Hall, A.: Increasing precipitation volatility in
- 567 twenty-first-century California, Nat Clim Chang, 8, 427–433, https://doi.org/10.1038/s41558-
- 568 018-0140-y, 2018.
- 569 Tateo, F.: Clay minerals at the paleocene-eocene thermal maximum: Interpretations, limits, and
- 570 perspectives, Minerals, 10, 1–16, https://doi.org/10.3390/min10121073, 2020.
- 571 Tipple, B. J., Pagani, M., Krishnan, S., Dirghangi, S. S., Galeotti, S., Agnini, C., Giusberti, L., and
- 572 Rio, D.: Coupled high-resolution marine and terrestrial records of carbon and hydrologic cycles

© Author(s) 2023. CC BY 4.0 License.





- 573 variations during the Paleocene Eocene Thermal Maximum (PETM), Earth Planet Sci Lett,
- 574 311, 82–92, https://doi.org/10.1016/j.epsl.2011.08.045, 2011.
- 575 Tipple, B. J., Berke, M. A., Doman, C. E., Khachaturyan, S., and Ehleringer, J. R.: Leaf-wax n-
- alkanes record the plant-water environment at leaf flush, Proc Natl Acad Sci U S A, 110, 2659–
- 577 2664, https://doi.org/10.1073/pnas.1213875110, 2013.
- 578 Tipple, B. J., Berke, M. A., Hambach, B., Roden, J. S., and Ehleringer, J. R.: Predicting leaf wax n-
- alkane 2H/1H ratios: controlled water source and humidity experiments with hydroponically
- 580 grown trees confirm predictions of Craig-Gordon model, Plant Cell Environ, 38, 1035–1047,
- 581 https://doi.org/10.1111/PCE.12457, 2015.
- 582 Vogel, M. M., Hauser, M., and Seneviratne, S. I.: Projected changes in hot, dry and wet extreme
- 583 events' clusters in CMIP6 multi-model ensemble, Environmental Research Letters, 15,
- 584 https://doi.org/10.1088/1748-9326/ab90a7, 2020.
- 585 Wakeham, S. G. and Pease, T. K.: Lipid Analysis in Marine Particle and Sediment Samples A
- Laboratory Handbook, 2004.
- 587 de Wet, C. B., Erhardt, A. M., Sharp, W. D., Marks, N. E., Bradbury, H. J., Turchyn, A. V., Xu, Y.,
- 588 and Oster, J. L.: Semiquantitative Estimates of Rainfall Variability During the 8.2 kyr Event in
- California Using Speleothem Calcium Isotope Ratios, https://doi.org/10.1029/2020GL089154,
- 590 16 February 2021.
- 591 Williams, A. P., Cook, E. R., Smerdon, J. E., Cook, B. I., Abatzoglou, J. T., Bolles, K., Baek, S. H.,
- 592 Badger, A. M., and Livneh, B.: Large contribution from anthropogenic warming to an emerging
- 593 North American megadrought, Science (1979), 368, 314–318, 2020.
- 594 Willis, K.J, McElwain, J. C.: The Evolution of Plants, OUP Oxford, 392 pp., 2002.
- 595 Wing, S. L., Harrington, G. J., Smith, F. a, Bloch, J. I., Boyer, D. M., and Freeman, K. H.: Transient
- 596 Floral Change and rapid global warming at the P/E boundary, Science (1979), 310, 993–996,
- 597 https://doi.org/10.1126/science.1116913, 2005.
- 598 Zachos, J. C., Dickens, G. R., and Zeebe, R. E.: An early Cenozoic perspective on greenhouse
- warming and carbon-cycle dynamics, Nature, 451, 279–283,
- 600 https://doi.org/10.1038/nature06588, 2008.
- 601 Zamora-Reyes, D., Broadman, E., Bigio, E., Black, B., Meko, D., Woodhouse, C. A., and Trouet,
- 602 V.: The Unprecedented Character of California's 20th Century Enhanced Hydroclimatic
- Variability in a 600-Year Context, Geophys Res Lett, 49,
- 604 https://doi.org/10.1029/2022GL099582, 2022.
- 605 Zhu, J., Poulsen, C. J., Otto-Bliesner, B. L., Liu, Z., Brady, E. C., and Noone, D. C.: Simulation of
- 606 early Eocene water isotopes using an Earth system model and its implication for past climate
- 607 reconstruction, Earth Planet Sci Lett, 537, 116164, https://doi.org/10.1016/j.epsl.2020.116164,
- 608 2020.
- 609 Zscheischler, J. and Lehner, F.: Attributing Compound Events to Anthropogenic Climate Change,
- 610 Bull Am Meteorol Soc, 103, E936–E953, https://doi.org/10.1175/BAMS-D-21-0116.1, 2022.

611